

Conditions for the Formation of First-Star Binaries

Masahiro N. Machida¹, Kazuyuki Omukai², Tomoaki Matsumoto³, and Shu-ichiro Inutsuka¹

ABSTRACT

The fragmentation process of primordial-gas cores during prestellar collapse is studied using three-dimensional nested-grid hydrodynamics. Starting from the initial central number density of $n_c \sim 10^3 \text{ cm}^{-3}$, we follow the evolution of rotating spherical cores up to the stellar density $n_c \simeq 10^{22} \text{ cm}^{-3}$. An initial condition of the cores is specified by three parameters: the ratios of the rotation and thermal energies to the gravitational energy (β_0 , and α_0 , respectively), and the amplitude of the bar-mode density perturbation (A_ϕ). Cores with rotation $\beta_0 > 10^{-6}$ are found to fragment during the collapse. The fragmentation condition hardly depends on either the initial thermal energy α_0 or amplitude of bar-mode perturbation A_ϕ . Since the critical rotation parameter for fragmentation is lower than that expected in the first star formation, binaries or multiples are also common for the first stars.

Subject headings: cosmology: theory — galaxies: formation — hydrodynamics — stars: formation

1. Introduction

More stars are in binaries or multiples than in singles in the solar vicinity (Duquennoy & Mayor 1992; Fischer & Marcy 1992). Is this also true of the first-generation stars? Being very massive ($\gtrsim 100M_\odot$; see e.g., Bromm & Larson 2004), first-star binaries, if they are formed, can contribute greatly as progenitors of gamma-ray bursts (Bromm & Loeb 2006; but see Belczynski et al. 2006 for the opposite view) or gravitational wave sources (Belczynski

¹Department of Physics, Graduate School of Science, Kyoto University, Sakyo-ku, Kyoto 606-8502, Japan; machidam@scphys.kyoto-u.ac.jp, inutsuka@tap.scphys.kyoto-u.ac.jp

²National Astronomical Observatory of Japan, Mitaka, Tokyo 181-8588, Japan; omukai@th.nao.ac.jp

³Faculty of Humanity and Environment, Hosei University, Fujimi, Chiyoda-ku, Tokyo 102-8160, Japan; matsu@i.hosei.ac.jp

et al.2004). However, binary formation in primordial gas has sometimes been considered unlikely, based on the fact that no cooling mechanism induces fragmentation of high-density ($\gtrsim 10^4 \text{cm}^{-3}$) cores (e.g., Ripamonti & Abel 2004).

Rotation can change this picture. Unlike the case of present-day star formation, where the angular momentum is effectively transported by magnetic braking (Basu & Mouschovias 1994) or outflow (Tomisaka 2002), in first-star formation, the magnetic field is extremely weak (e.g., Takahashi et al. 2005; Ichiki et al. 2006) and thus expected to play little role in the angular momentum transport. With conserved angular momentum, the effect of rotation is enhanced in the course of the collapse of the core, and a disk is expected to form. Do such disks fragment to binaries or multiples? To answer this question, by three-dimensional hydrodynamics, Saigo et al.(2004) demonstrated that primordial-gas cores with rapid rotation indeed fragment into binaries. Nonetheless, their analysis is not satisfactory in the following respects: First, they started calculation at rather high density $\sim 10^{10} \text{cm}^{-3}$, and thus were forced to assume somewhat ad hoc initial conditions of high angular-momentum cores. In practice, the angular momentum might have been transferred by the non-axisymmetric structure before reaching this density. In addition, they presented only one model of a core experiencing fragmentation. Recently, Clark, Glover, & Klessen (2007) performed three-dimensional hydrodynamical simulation of star formation in a low-metallicity turbulent medium and found that rotation causes fragmentation even in metal-free gas, as suggested by Saigo et al. (2004). However, they do not discuss fragmentation conditions of the cores in their analysis.

In this paper, we calculated the evolution of primordial-gas rotating cores for twenty orders of magnitude in the density contrast, starting from the formation of dense cores ($n \simeq 10^3 \text{cm}^{-3}$) up to stellar-core formation ($n \simeq 10^{22} \text{cm}^{-3}$). We adopt a realistic equation of state derived by Omukai et al. (2005), rather than a simple polytropic relation $P \propto \rho^{1.1}$ used by Saigo et al. (2004). To determine the fragmentation conditions for the primordial-gas cores, we calculated 38 models with different values of rotation, thermal energy, and amplitude of non-axisymmetric perturbation. Using the initial ratio of rotation to gravitational energies β_0 , the conditions for a primordial-gas core to fragment are $\beta_0 > 10^{-6}$, while dependence of these conditions on either the thermal energy or the amplitude of non-axisymmetric perturbation is very weak. These conditions are easily satisfied in the first-star forming cores, and thus binary formation is also important for first stars.

The following is the plan of this paper. In this paper, after first summarizing the basics of our model in §2, we describe the numerical method in more detail in §3. We present the results for the initially quasi-stable cores in §4, and those for highly gravitationally unstable cores in §5. The fragmentation criterion is examined in §6. Finally in §7, summary and

discussions are presented.

2. Model Settings

We solve the equations of hydrodynamics including self-gravity:

$$\frac{\partial \rho}{\partial t} + \nabla \cdot (\rho \mathbf{v}) = 0, \quad (1)$$

$$\rho \frac{\partial \mathbf{v}}{\partial t} + \rho (\mathbf{v} \cdot \nabla) \mathbf{v} = -\nabla P - \rho \nabla \phi, \quad (2)$$

$$\nabla^2 \phi = 4\pi G \rho, \quad (3)$$

where ρ , \mathbf{v} , P , and ϕ denote the density, velocity, pressure, and gravitational potential, respectively. For gas pressure, we use a barotropic relation that approximates the result for a primordial-gas core by Omukai et al. (2005). Omukai et al. (2005) studied the thermal evolution of low-metallicity star-forming cores using a simple one-zone model for the dynamics, where the core collapses approximately at the free-fall rate and the size of the core is about the Jeans length, as in the Larson-Penston self-similar solution (Penston 1969; Larson 1969). On the other hand, detailed thermal and chemical processes in primordial gas are treated. Their result and our fit to it are plotted against the number density in Figure 1. To emphasize variations of pressure with density, we plot P/n , which is proportional to the gas temperature divided by the mean molecular weight.

As an initial condition of the cores, we use a density profile increased by a factor of $f (\gtrsim 1)$ from that of the critical Bonnor-Ebert (BE) sphere (Ebert 1955; Bonnor 1956). For the critical BE sphere, the central number density is $n_{c,0} = 1 \times 10^3 \text{ cm}^{-3}$, and the initial temperature is about 250K at the center from our adopted barotropic relation (Fig.1). The critical radius of the BE sphere is $R_c = 6.45 c_s / \sqrt{4\pi G \rho_{BE}(0)} = 6.5 \text{ pc}$. Outside this radius, uniform gas density of $n_{BE}(R_c) = 71.1 f \text{ cm}^{-3}$ is assumed. The total mass contained in the critical BE sphere is $M_c = 6.2 \times 10^3 M_\odot$, and thus our initial core is f times more massive than this value. In Figure 2, the profiles of density and cumulative mass of the initial state are plotted.

Initially the core rotates rigidly with angular velocity Ω_0 around the z -axis. The initial models are characterized by three non-dimensional parameters: the ratio of the thermal to gravitational energy (α_0), the ratio of the rotation to gravitational energy (β_0), and the amplitude of the non-axisymmetric perturbation (A_ϕ). The models with different (α_0, β_0) are constructed by changing the initial density enhancement factor (f) and angular velocity (Ω_0). Parameters α_0 and β_0 are summarized in Table 1, along with the density enhancement

factor f . Non-axisymmetric density perturbation of the $m = 2$ mode, i.e., bar mode, is added to the initial cores. In summary, the density profile of the core is denoted as

$$\rho(r) = \begin{cases} \rho_{\text{BE}}(r) (1 + \delta\rho) f & \text{for } r < R_c, \\ \rho_{\text{BE}}(R_c) (1 + \delta\rho) f & \text{for } r \geq R_c, \end{cases} \quad (4)$$

where $\rho_{\text{BE}}(r)$ is the density distribution of the critical BE sphere, $\delta\rho$ is the non-axisymmetric density perturbation. For the bar($m = 2$)-mode,

$$\delta\rho = A_\phi(r/R_c) \cos 2\phi \quad \text{for } r \geq R_c, \quad (5)$$

where A_ϕ is the amplitude of the perturbation. We use A_ϕ as a free parameter, and study cases with $A_\phi = 0.001 - 0.3$ (see Table 1). To disturb the $m = 2$ symmetry in a high-density region (for detail, see Matsumoto & Hanawa 2003), we add the $m = 3$ mode of velocity perturbation as

$$\Omega = \Omega_0 [1 + \Omega_3(r/R_c) \cos 3\phi]. \quad (6)$$

The amplitude Ω_3 is set to 10^{-5} in all the models.

3. Numerical Method

We adopt a nested grid method (for details, see Machida et al. 2005a; 2006a) to obtain high spatial resolution near the center. Each level of a rectangular grid has the same number of cells ($= 256 \times 256 \times 16$), with the cell width $h(l)$ which is a function of grid level l . The cell width is halved at each increment of the grid level. The highest level of grids increases with time: a new finer grid is generated whenever the minimum local Jeans length λ_J falls below $8 h(l_{\text{max}})$, where $h(l_{\text{max}})$ is the cell width of the current finest grid. The maximum level of grids is restricted to $l_{\text{max}} \leq 30$. The generation of a new grid at the density maximum ensures the Jeans condition of Truelove et al. (1997) with a margin-of-safety factor of two. We begin our calculations with four grid levels (i.e., $l_{\text{max}} = 4$). The box size of the initial finest grid $l = 4$ is chosen to be $2R_c$, where R_c is the radius of the critical BE sphere. The coarsest grid ($l = 1$) thus has a box size of $2^4 R_c$. The mirror symmetry with respect to the $z=0$ is imposed. At the boundary $r = 2^4 R_c$, the ambient gas is set to rotate with angular velocity Ω_0 (for more detail, see Matsumoto & Tomisaka 2004).

4. Evolution of quasi-hydrostatic cores

According to numerical simulations (Bromm et al. 1999; Abel et al. 2002; Yoshida et al. 2006), in the case of first star formation, self-gravitating isolated cores form at the number

density $10^3 - 10^4 \text{ cm}^{-3}$, where temperature takes its minimum (see Fig. 1). These cores are close to the hydrostatic equilibrium, i.e., $\alpha_0 \simeq 1$, which is a general property of cores forming by gravitational instability. In this section, we study such cases as $\alpha_0 \simeq 1$, and we defer the effect of different α_0 to Sec. 5.

In Figure 3, the final states of our simulation for the cores with $\alpha_0 \simeq 1$ are presented for various combinations of initial rotation parameter β_0 and bar-mode perturbation A_ϕ . The model parameters ($\alpha_0, \beta_0, A_\phi$) are summarized in Table 1 (models 1-24 for those in Fig. 3). Also presented in Table 1 are the number density (n_f) at fragmentation, the number of fragments, the separation between the fragments at the end of the calculation, and the mode of fragmentation (i.e., ring or bar-mode; see below). Among models presented in Figure 3, for models 1-4 with the highest rotation parameter ($\beta_0 = 0.1$), we need to adopt values of α_0 ($= 0.7$) smaller than in the other models ($\alpha_0 = 0.83$) to initiate the collapse. In Figure 3 we see that cores with rotation $\beta_0 \geq 10^{-5}$ fragment for all values of bar-mode perturbation A_ϕ in our calculated range.

It is known that cores fragment only after they become either thin disks or elongated filaments (Tohline 1980). Correspondingly, the mode of fragmentation can be classified into two types (See Fig. 4). One is ring-mode fragmentation induced by rotation, and the other is bar-mode fragmentation induced by bar instability (Machida et al. 2004; 2005b). The mode of fragmentation is determined by the axis ratio. If the axis ratio does not grow sufficiently during the collapse, the core becomes ring-like due to the rotation and then fragments into pieces (i.e., *ring-mode fragmentation*). On the other hand, a core with small rotation but with a large enough bar-mode perturbation results in an elongated structure, and fragments due to the bar instability (i.e., *bar-mode fragmentation*). For example, models in the second column of Figure 3 experience ring-mode fragmentation, while in the fourth column where $\beta_0 \geq 10^{-3}$ the cores fragment through the bar mode. The mode of fragmentation determines the fate of the fragments to some extent. Survival of fragments and formation of binary/multiple are easier in the ring mode due to large orbital angular momentum between the fragments, while in the bar mode, they tend to merge, and fragmentation is repeated in the merged core (Matsumoto & Hanawa 2003; Machida et al. 2005b).

Our calculations are terminated when either the Jeans condition is violated in the maximum ($l_{\text{max}} = 30$) grid level or the maximum density exceeds $n_c \gtrsim 10^{22} \text{ cm}^{-3}$. Since the former situation easily occurs when the fragments leave the center, where the grid is finest, after the fragmentation we can continue calculation only for a short duration. Due to this limitation, our calculation covers only a rather low-density range for models with high β_0 (models 1-4), where fragmentation occurs at low densities ($n_c \simeq 10^{11} \text{ cm}^{-3}$). In these models, the cores might experience another episode of fragmentation if we continued calculation

further. For the other models in Figure 3, our calculation covers the entire evolution until the stellar core formation after the equation of state becomes adiabatic.

4.1. Case Studies

In this section, we see the evolution of cores in models 22, 6 and 8, which are examples of a non-fragmenting core, a core fragmenting in the ring-mode, and in the bar-mode, respectively.

We define here the following three quantities which describe the state of cores at a given time for later use. To examine the evolution of rotation velocity around the center, we use angular velocity normalized by the free-fall timescale; $\omega_c \equiv \Omega_c / (4\pi G \rho_c)^{1/2}$. Hereafter, we call this quantity the normalized angular velocity. For a rigidly rotating sphere with uniform density, the normalized angular velocity is related to the ratio of the rotation to the gravitational energy (β_c) by

$$\beta_c = \frac{\Omega_c^2 R^3}{3GM} = \frac{\Omega_c^2}{4\pi G \rho_c}, \quad (7)$$

where R and M are the radius and mass of the sphere, respectively. Even when the core deviates somewhat from the sphere in the course of the collapse, equation (7) remains a good indicator for rotation (Machida et al. 2005a; 2006a). Also, to see the degree of deformation from a sphere and approach to a disk, we define oblateness of the core as $\varepsilon_{\text{ob}} \equiv (h_l h_s)^{1/2} / h_z$, where h_l , h_s , and h_z are, respectively, lengths of the major, minor, and z -axes derived from the moment of inertia for the high-density gas $\rho \geq 0.1\rho_c$, i.e., density higher than 10% of the central value. Also, as the degree of deviation from a circle when projected on the $x - y$ plane, the axis ratio is defined as $\varepsilon_{\text{ar}} \equiv h_l / h_s - 1$.

4.1.1. Non-fragmenting Core: Model 22

As an example of cores that do not experience fragmentation, we describe the evolution in model 22, whose parameters are $(\alpha_0, \beta_0, A_\phi) = (0.83, 10^{-6}, 10^{-2})$. In this case, a hydrostatic core (“stellar core”) forms without fragmentation. This structure is shown in several evolutionary stages in Figure 5. Panel *a* shows the initial state. We adopt the critical BE sphere as an initial state (Sec.2), but add 1% of density perturbation for triggering gravitational collapse. The initial density contrast is thus 14 between the center and the ambient medium.

Since the rotation is very slow ($\beta_0 = 10^{-6}$) in this model, the collapse becomes almost

spherically symmetric in the early phase, as seen in panels *b-d*. In fact, the infall motion is almost radial, i.e., the radial component of the gas velocity is much larger than the azimuthal component, $v_r \gg v_\phi$. The effect of rotation becomes important with the collapse, and deviation from the spherical collapse becomes obvious around $n_c \sim 10^{17} \text{ cm}^{-3}$ (see Figs. 5*e*, where $n_c = 7.1 \times 10^{18} \text{ cm}^{-3}$). Now the azimuthal velocity is comparable to the radial one ($v_\phi \simeq v_r$), and the gas falls to the center with significant rotation.

In Figure 6, we plot the normalized angular velocity (Fig. 6*a*), oblateness (Fig. 6*b*), and axis ratio (Fig. 6*c*) against the central number density for this case (model 22) along with those with different β_0 but the same $A_\phi = 10^{-2}$ (models 2, 6, 18) for comparison. Those quantities are calculated for the central region whose density is higher than 10% of the central value.

For the spherical rigid-body rotation, angular velocity increases as $\Omega_c \propto n_c^{2/3}$ owing to the conservation of angular momentum, and thus normalized angular velocity $\omega_c \propto n_c^{1/6}$. In model 22, this spherical collapse phase continues until $n_c \sim 10^{19} \text{ cm}^{-3}$, where the saturation of the normalized angular momentum around $\omega_c \simeq 0.2 - 0.3$ is observed. This indicates that a thin disk begins to form at the center, for which the normalized angular velocity increases as $\omega_c \propto n_c^{\gamma-1/2}$, which is almost constant in our case where $\gamma \simeq 1.1$. This can be derived from the conservation of specific angular momentum $j/M = \pi\varpi^2\Omega_c/\pi\varpi^2\Sigma = \text{const.}$, where ϖ is the radius of the disk and the column density Σ can be expressed as $\Sigma \simeq \rho H$ using the disk scale height $H \simeq c_s/\sqrt{G\rho} \propto \rho^{\gamma-1/2}$, where c_s is the sound speed.

The formation of the disk can be seen in the behavior of the oblateness. For $n_c \lesssim 10^{19} \text{ cm}^{-3}$, the collapse is spherical and the oblateness remains close to unity (see Fig. 6*b*). After the normalized angular momentum reaches the saturation level and the radial collapse is hindered to some extent by centrifugal force, the oblateness begins to increase. When the central density reaches $n_c = 3 \times 10^{21} \text{ cm}^{-3}$, a stellar core with an initial mass of $6.7 \times 10^{-3} M_\odot$, forms at the center, surrounded by a shock. Figure 5*f* shows the structure immediately after the stellar core formation. In this figure, the surface of the stellar core is indicated by the thick black line. The density and mass of the stellar core at the formation in our model are well in agreement with the results of Omukai & Nishi (1998), who calculated the collapse of a primordial star-forming core including detailed radiative and chemical processes under the assumption of spherical symmetry. After the formation, the stellar core becomes round in shape and the oblateness stops increasing. The oblateness can grow remarkably only after the saturation of ω_c and before the formation of the stellar core. In this model, the saturation of ω_c occurs only slightly before the stellar core formation, owing to a small initial rotation β_0 . Thus, the core does not become oblate enough to fragment in the ring mode (see Sec 4.1.2).

Next, we see the growth of the bar-mode perturbation ε_{ar} in Figure 6c. Recall that we add 1% of bar-mode density perturbation to the initial state, i.e., $A_\phi = 10^{-2}$. The axis ratio of the core in model 22 remains very small throughout the evolution ($\varepsilon_{\text{ar}} \lesssim 10^{-2}$). The growth of the bar-mode perturbation can be described by a linear perturbation theory developed by Hanawa & Matsumoto (2000) and Lai (2000) for small deviation from the spherical self-similar solution. They showed that a collapsing spherical core with a polytropic index γ is unstable against a bar-mode perturbation when $\gamma \leq 1.097$, and the perturbation of the bar mode grows as $\varepsilon_{\text{ar}} \propto n_c^s$, with s being a constant for a given γ . For the isothermal case ($\gamma = 1$), for example, $s = 0.177$ ($\simeq 1/6$): the growth rate is the same as that of the normalized angular velocity ω_c (Hanawa & Matsumoto 1999). For more reference, see Figure 14 of ?, where the power index s is shown as a function of γ . In our case, the polytropic index ranges in $1 \lesssim \gamma \lesssim 1.15$ (see Fig. 1), corresponding to the range of the power index $-0.4 \lesssim s \lesssim 0.2$. For $10^8 \text{ cm}^{-3} \lesssim n_c \lesssim 10^{16} \text{ cm}^{-3}$, γ becomes $\simeq 1$, and then ε_{ar} grows (Fig. 6c), although the growth rate is somewhat lower than in the isothermal case.

We show the evolution of the radial density distribution averaged around the rotation axis in Figure 7a. With only slow rotation, the evolution of both density and velocity distributions resembles closely a result of the spherically symmetric calculation (Omukai & Nishi 1998). The collapse proceeds in a self-similar way with a polytropic index $\gamma \simeq 1.1$: the evolution of density distribution resembles closely the Larson-Penston self-similar solution, whose density gradient in the envelope is $\propto r^{-2/(2-\gamma)} \simeq r^{-2.2}$. The appearance of a shock front due to the stellar core formation is seen in the velocity distribution at state 6 (Figure 7b).

4.1.2. Ring-mode Fragmentation: Model 6

Here, we see an example of a core with rapid rotation. In Figure 8, we show the evolutionary sequence of model 6, whose parameters are $(\alpha_0, \beta_0, A_\phi) = (0.83, 10^{-2}, 10^{-2})$. Rotation energy of this model is 10^4 times larger than that of model 22 above, while the other parameters A_ϕ and α_0 are the same. In contrast to model 22, where the collapse is almost spherical, here rotation plays a major role. After some contraction, the core becomes ring-like, owing to the centrifugal support, and eventually fragments.

The core is still spherical early in the evolution (Fig. 8a; $\varepsilon_{\text{ob}} = 1.2$, $n_c = 3 \times 10^7 \text{ cm}^{-3}$). With further contraction, rotation makes it oblate perpendicular to the z -axis (Fig. 8b; $\varepsilon_{\text{ob}} = 3.8$, $n_c = 2 \times 10^{11} \text{ cm}^{-3}$). As in model 22 above, the normalized angular velocity grows initially as $\omega_c \propto n_c^{1/6}$ and then saturates around $\omega_c \simeq 0.2 - 0.3$ (Fig. 6a). In this model, however, the saturation occurs earlier at $n_c \simeq 10^7 \text{ cm}^{-3}$ than in model 22 ($\simeq 10^{19} \text{ cm}^{-3}$), owing to faster initial rotation. The normalized angular velocity oscillates around the saturation value

$\omega_c \simeq 0.2 - 0.3$ thereafter, which corresponds to $\beta_c = 0.04 - 0.09$ by the relation (7). In other words, after the ratio β_c reaches a certain level of $0.04 - 0.09$, the core contracts, keeping a constant ratio between the centrifugal and gravitational forces near the center. The approach to a disk-like configuration can be observed in the increase of oblateness (the dashed line in Fig. 6b) after the saturation of the normalized angular velocity. The oblateness also saturates at $\varepsilon_{\text{ob}} \simeq 10$ and then oscillates after that. Note that the face-on view on the $x - y$ plane remains quite circular even after the thin disk formation. For example, the axis ratio ε_{ar} is $\sim 10^{-3}$ at the time of Panels *a* and *b* of Figure 8.

As can be seen in the middle and lower panels of Figure 8c, two disks are nested, and each disk is sandwiched by horizontal shocks above and below. The outer and inner shocks exist at $z = \pm 0.2$ AU and $z = \pm 0.05$ AU, respectively. Outside the outer disk, cavities exist along the z -axis. The emergence of the shocks is related to the oscillatory behavior of oblateness after its saturation: a pair of shocks appear whenever the core becomes maximally oblate and then bounces back (Matsumoto et al. 1997; Machida et al. 2005a, 2006a). In this model, two maxima of the oblateness appear around $n_c \simeq 10^{13} \text{ cm}^{-3}$ and 10^{17} cm^{-3} (Fig. 6b). Correspondingly, the outer shock appears at $n_c \simeq 10^{13} \text{ cm}^{-3}$ and the inner shock at $n_c \simeq 10^{17} \text{ cm}^{-3}$.

The axis ratio of an oblate core grows faster than the linear theory predicts (see Fig. 6c). Although the core deforms to an ellipsoid by this effect (Fig. 8c; $n_c \simeq 5 \times 10^{18} \text{ cm}^{-3}$), the deformation is not sufficient owing to the initial small value of A_ϕ . Consequently, the core eventually transforms to a ring rather than to an ellipsoid, and fragments at $n_c \simeq 7 \times 10^{18} \text{ cm}^{-3}$ into two pieces with almost equal mass of $\simeq 1 \times 10^{-2} M_\odot$ (Fig. 8d). The rapid drop of the normalized angular velocity at $n_c \simeq 10^{18} \text{ cm}^{-3}$ (dashed line of Fig. 6a) can be attributed to a rapid increase in the oblateness of the core (i.e., deformation to a flat disk shape), and consequent redistribution of the angular momentum of the core due to this non-axisymmetric density distribution.

When the density reaches $n \simeq 10^{20} \text{ cm}^{-3}$, a stellar core forms in each fragment. Each core is surrounded by a shock (Fig. 8e and f). Although the stellar cores are initially ellipsoidal in shape (Fig. 8e), they subsequently become spherical (Fig. 8f). The mass of each stellar core reaches $3.1 \times 10^{-3} M_\odot$ each at the end of the calculation. The two cores continue to part, and the final separation is $R_{\text{sep}} = 0.36$ AU. Although the main bodies of the cores approach spherical in shape after the formation, their envelopes become more elongated, like tails. They eventually become detached (see the upper panel of Fig. 8f). Having density peaks inside [at $(x, y) \simeq (\pm 0.17, \pm 0.24)$], these “tails” may hatch other stellar cores.

The evolutionary sequences of number density and velocity before fragmentation are shown in Figures 9a and b, respectively. Despite the deformation to a disk-like structure,

the evolution of the core is well described by the Larson-Penston self-similar solution until the fragmentation (c.f., Saigo et al. 2000). Similar behavior in the isothermal collapse has been found by Matsumoto et al. (1997).

4.1.3. Bar-mode Fragmentation: Model 8

Here, we see model 8, whose parameters are $(\alpha_0, \beta_0, A_\phi) = (0.83, 10^{-2}, 0.3)$. The initial core has non-axisymmetric perturbation 30 times larger than in model 6, while the other parameters are the same. The evolutionary sequence of this model is shown in Figure 10. A non-axisymmetric structure, or a “bar”, already appears in an early phase. The bar becomes more elongated with collapse and eventually fragments. Evolution of the normalized angular velocity (ω_c), oblateness (ε_{ob}), and axis ratio (ε_{ar}) are plotted in Figures 11*a*, *b*, and *c* (dashed lines).

Like in the previous examples, the central portion evolves keeping a spherical shape until disk formation (Fig. 10*a*; $n_c = 4.7 \times 10^8 \text{ cm}^{-3}$). Evolution of both the normalized angular velocity and the oblateness is also very similar to those of previous models (Fig. 6*a*, *b*). The oblateness saturates around $\varepsilon_{ob} \simeq 7$ at $n_c \simeq 10^{13} \text{ cm}^{-3}$ and it subsequently oscillates (dashed lines of Fig. 11*b*). When the oblateness reaches its maxima, a thin disk bounded by shocks forms, as in model 6 (middle and lower panels of Fig. 10*c*). However, owing to its high initial value, the non-axisymmetric perturbation has grown significantly by the time of the disk formation, i.e., the saturation of ω_c . The growth of the axis ratio is accelerated even more after the disk formation and a clear bar-like structure develops (Fig. 10*d*). The bar elongates further and eventually fragments at $n_c = 1.9 \times 10^{19} \text{ cm}^{-3}$. By this moment, the axis ratio reaches $\varepsilon_{ar} = 31.4$. This value is similar to the axis ratio at the fragmentation found by Tsuribe & Omukai (2006), whose calculation is limited to non-rotating cases. Inside the fragments, the stellar cores form after the equation of state becomes adiabatic (Fig. 10*e*, *f*).

The separation between the fragments is $R_{sep} = 0.4 \text{ AU}$ and the mass of a fragment is $3 \times 10^{-2} M_\odot$ at the end of the calculation. The fragmentation epoch and separation are similar to those in model 6, which implies that the initial amplitude of the non-axisymmetric perturbation does not affect these quantities. In contrast to the case of model 6, the fragments approach each other after fragmentation as a result of their small orbital angular momentum. Judging from the final state of our calculation, merger of the fragments appears inevitable although it has not yet occurred within our run.

4.2. Effect of rotation parameter β_0

In this section, we summarize effects of different initial rotation parameters β_0 on the evolution. As examples, in the second column of Figure 3, we compare six models 2, 6, 10, 14, 18 and 22, which have different β_0 ($= 10^{-6} - 0.1$) but with the same A_ϕ ($= 10^{-2}$). The normalized angular velocities, oblatenesses, and axis ratios are plotted in Figures 6a, 6b, 6c for four of them (models 2, 6, 18 and 22).

Except for the fastest rotation case of model 2, normalized angular velocities increase in the low density regime as $\omega_c \propto n_c^{1/6}$, which is the spherical collapse relation. The normalized angular velocity saturates around $\omega_c \simeq 0.2 - 0.3$ in all cases. Note that the saturation values of ω_c are similar in all models, although the epoch of saturation is earlier (i.e., at lower densities) for those with larger initial rotation. After the saturation, the normalized angular velocity oscillates around the saturation value $\omega_c \simeq 0.2 - 0.3$ until fragmentation. Similar behaviors of the angular velocity have been found by Matsumoto & Hanawa (2003) and Machida et al. (2006a), who showed that the normalized angular velocity converges to a certain value in the self-similar collapse. In the case with the fastest rotation (model 2; $\beta_0 = 0.1$), since the saturation level $\omega_c \simeq 0.2 - 0.3$ ($\beta \simeq 0.04 - 0.09$) has been reached from the onset, the normalized angular velocity remains almost constant until fragmentation.

The shape of the cores remains almost spherical, namely, the oblateness is small $\varepsilon_{\text{ob}} \simeq 1$, until the saturation of the normalized angular velocity. It is only after the saturation of ω_c that the oblateness begins to increase remarkably (Fig. 6a, b). In the largest rotation case of model 2, the oblateness can increase from the onset since the saturation level of ω_c has already been attained already in the initial state. Like ω_c , the oblateness also saturates at $\varepsilon_{\text{ob}} \simeq 10$ and oscillates thereafter around this value until fragmentation.

From this behavior of oblateness, we conclude that the saturation of ω_c to $\simeq 0.2 - 0.3$ is necessary for the formation of a thin ($\varepsilon_{\text{ob}} \simeq 10$) disk. A thin disk can continue collapsing with conserved angular momentum for effective adiabatic index $\gamma \leq 1$ (Saigo et al. 2000). For $\gamma > 1$, the central portion of the disk eventually supported by rotation and its collapse is halted, leading to fragmentation of the disk. In our case, where $\gamma > 1$ in most of the density range, such a thin disk eventually fragments. Thus *the saturation of ω_c is a prerequisite for fragmentation of the core.*

The evolution of the axis ratio is presented in Figure 6c. Also shown by a straight line is that for the isothermal gas in the linear theory $\varepsilon_{\text{ar}} \propto n_c^{1/6}$ (see Sec. 4.1.1). Before the formation of thin disks, the axis ratios decrease for $n_c \lesssim 10^8 \text{ cm}^{-3}$ and then increase in higher densities by obeying the linear theory. After the flat disk with $\varepsilon_{\text{ob}} > 7 - 10$ is formed, the growth rate of the axis ratio is more enhanced than the linear theory predicts. In fact,

the axis ratio continues to increase even when the polytropic index γ is larger than 1.1 for $n_c > 10^{16} \text{ cm}^{-3}$. A similar effect is known in the isothermal collapse: a collapsing disk exhibits a larger growth rate of the bar-mode perturbation than a sphere (Nakamura & Hanawa 1997; Matsumoto & Hanawa 1999).

Since fragmentation occurs only after the disk formation, cores with larger initial rotation tend to fragment at lower densities, and the separations between fragments are wider. For example, in model 2 ($\beta_0 = 0.1$), with the fastest rotation, the fragmentation density is $2 \times 10^{11} \text{ cm}^{-3}$ and the separation between the fragments is $R_{\text{sep}} = 600 \text{ AU}$ at the end of the calculation, while in model 18 ($\beta_0 = 10^{-5}$), they are $6 \times 10^{20} \text{ cm}^{-3}$ and 0.09 AU , respectively. For slower rotation ($\beta_0 = 10^{-6}$; model 22), fragmentation does not take place. We also calculated a few cases with even smaller rotation energies and confirmed that the cores do not fragment.

4.3. Effect of bar-mode perturbations

Next, in order to study the effect of initial bar-mode perturbation A_ϕ , we focus on four models (models 5-8) with the same $\beta_0 (= 10^{-2})$ but with different $A_\phi (= 0.001, 0.01, 0.1, \text{ and } 0.2 \text{ for models 5, 6, 7, and 8, respectively})$. Their final states are presented in the second row of Figure 3.

With increasing A_ϕ , the mode of fragmentation changes from the ring to bar mode. In models with small $A_\phi (\leq 0.01; \text{ models 5 and 6})$, a ring forms near the center owing to centrifugal force and subsequently fragments into several pieces. On the other hand, for larger $A_\phi (\geq 0.1; \text{ models 7 and 8})$, the central region transforms from a disk to a bar-like structure before fragmentation. In model 7, the core takes a ring-like structure near the center whereas a bar-like one in a larger scale. The model with largest A_ϕ (Model 8) clearly takes a bar-like structure.

Whether fragmentation occurs or not appears to be solely determined by the rotation parameter β_0 . Cores with $\beta_0 > 10^{-6}$ always experience fragmentation before the formation of stellar cores. In addition, fragmentation epoch and separation between fragments depend only weakly on bar-mode perturbation A_ϕ . The fragmentation density n_f (i.e., epoch) ranges within an order of magnitude despite more than two orders of magnitude difference in A_ϕ : $n_f = 4 \times 10^{18} \text{ cm}^{-3}$ ($A_\phi = 0.001$; model 5), $7 \times 10^{18} \text{ cm}^{-3}$ (0.01; model 6), $7 \times 10^{18} \text{ cm}^{-3}$ (0.1; model 7), and $2 \times 10^{19} \text{ cm}^{-3}$ (0.2; model 8). We can see a weak trend that for larger A_ϕ , the fragmentation densities are higher. The larger bar-mode perturbation A_ϕ extracts more angular momentum from the central region, thereby delaying formation of a quasi-rotation-

supported disk and thus fragmentation.

The evolution of normalized angular velocity ω_c , oblateness ε_{ob} , and axis ratio ε_{ar} are shown in Figures 11*a*, *b*, *c* for models 5, 6, 7, and 8. With the same β_0 , evolutionary tracks for both ω_c and ε_{ob} are very similar for all these models until $n_c \simeq 10^{15} \text{ cm}^{-3}$ (Fig. 11*a*, *b*). For higher but still below fragmentation densities ($n_c \simeq 10^{15} - 10^{18} \text{ cm}^{-3}$), these tracks deviate from each other slightly owing to different shapes of the cores around the center (Fig. 3): disks remain highly circular in low A_ϕ models (5, 6 and 7), while an elongated bar forms in model 8 with high A_ϕ . As seen in Figure 11*c*, all the curves for ε_{ar} have the same shape and are only shifted upward or downward in relation to one another. That is, their growth rates are common but initial values are different. Fragmentation occurs via the ring mode in models 5-7 while via the bar-mode in model 8. At the fragmentation, the axis ratios are less than unity for models 5-7 ($\varepsilon_{ar} = 4.2 \times 10^{-2}$, 0.47, and 0.46 for models 5, 6, and 7, respectively), whereas it reaches as high as 31.4 for model 8.

In summary, the initial amplitude of bar-mode perturbation does affect the fragmentation mode, but the fragmentation epoch and separation of fragments are mostly determined by the rotation parameter β_0 .

5. Evolution of Highly Unstable Cores: Effect of initial thermal energy α_0

In the previous section, we investigated the evolution of cores with thermal energy comparable to gravitational energy ($\alpha_0 \approx 1$). Although this setting is probably most realistic for initial cores according to numerical simulations of gravitational fragmentation (e.g., Bromm et al. 2002; Yoshida et al. 2006), to see dependence of core evolution on initial thermal energy parameter α_0 , we study cases with $\alpha_0 \ll 1$ in this section.

Figure 12 shows the core structure at the end of the calculation for models 25-28. These models have the same initial rotation parameters ($\beta_0 = 10^{-3}$) and bar-mode perturbations ($A_\phi = 0.01$), but different thermal energies (α_0). Figure 13 shows the evolution of normalized angular velocity ω_c , oblateness ε_{ob} , and axis ratio ε_{ar} . The difference in α_0 hardly affects the evolution of ω_c and ε_{ob} , although, for models with smaller α_0 , both the ω_c and ε_{ob} saturate at slightly higher densities and at slightly higher values (Fig. 13*a*, *b*). On the other hand, the axis ratios ε_{ar} evolve quite differently among these models, in particular, in low densities $n_c \lesssim 10^{10} \text{ cm}^{-3}$ (Fig. 13*c*): ε_{ar} increases more for the lower α_0 cores. For higher densities, where the evolution of the cores already converge to the self-similar solution, the growth rate of ε_{ar} becomes the same for all the models, but this convergence occurs later for the lower

α_0 cores. Therefore, cores with smaller α_0 tend to have larger ε_{ar} , and then to fragment in the bar mode. For example, in models 25 and 26 with small α_0 ($=0.2, 0.4$), the bar-mode perturbation grows sufficiently and the cores fragment in the bar mode (Fig. 12*a, b*), while in models 27 and 28 ($\alpha_0 = 0.6$ and 0.8), fragmentation occurs in the ring mode (Fig. 12*c, d*).

6. Fragmentation Condition

As seen in Figure 3, the condition for fragmentation appears to be

$$\beta_0 > \beta_{\text{crit}} \sim 10^{-6} - 10^{-5}, \quad (8)$$

i.e., fragmentation occurs if the initial core has rotation energy 10^{-6} - 10^{-5} times the gravitational energy. Or, in terms of angular velocity of the initial core, this can be rewritten as

$$\Omega_0 > 3.67 \times 10^{-17} \left(\frac{n_0}{10^3 \text{ cm}^{-3}} \right)^{2/3} \text{ s}^{-1}, \quad (9)$$

where Ω_0 , and n_0 are the angular velocity and the central number density of the initial core, respectively, and we set $\beta_{\text{crit}} = 10^{-6}$. The dependence of equation (9) on the density comes from the fact that the angular velocity increases $\Omega \propto n_c^{2/3}$ in the case of a spherically collapsing core.

Next, we present a physical explanation for the fragmentation condition (8). As in Sec.4.2 and 4.3, the formation of a thin disk with oblateness $\varepsilon_{\text{ob}} \simeq 10$ is necessary for fragmentation. This must be attained before the equation of state becomes adiabatic at $n_c \simeq 10^{20} \text{ cm}^{-3}$ since the core becomes spherical and fragmentation is prohibited thereafter. The oblateness begins to grow remarkably only after the normalized angular velocity becomes close to the saturation value $\simeq 0.2 - 0.3$, and the level of $\varepsilon_{\text{ob}} \simeq 10$ is reached after further contraction of about four or five orders of magnitude in density. Therefore, as a condition for fragmentation, the normalized angular velocity must reach the saturation value ($\omega_c \simeq 0.2 - 0.3$, or $\beta_c \simeq 0.1$) before $\sim 10^{15} - 10^{16} \text{ cm}^{-3}$. By using the relation $\beta_c = \sqrt{\omega_c} \propto n_c^{1/3}$ for the spherical collapse, this can be translated to that on initial (i.e., at $\simeq 10^3 \text{ cm}^{-3}$) rotation parameter as $\beta_0 > (0.5 - 1) \times 10^{-5}$. This condition coincides well with our empirical relation (8).

In deriving the above condition, we neglect angular momentum transfer before the formation of a thin disk. As seen in Sec. 4.3, with the higher the bar-mode perturbation A_ϕ , the more angular momentum is transported. Thus, cores with higher initial A_ϕ would need higher β_0 for fragmentation to compensate the angular momentum transfer. This effect appears to be modest and is not observed clearly in our calculation.

7. Summary and Discussion

We have studied the gravitational collapse of zero-metallicity star-forming cores for different initial conditions, which are specified by the following three parameters, i.e., thermal energy, rotation energy, and amplitude of non-axisymmetric perturbations. Since the thermal energy of star-forming cores is expected to be similar to the gravitational energy, particular attention is paid to such cores. Initial conditions of the cores where fragmentation occurs are surveyed. We found that the cores with initial rotation energy higher than $10^{-6} - 10^{-5}$ times the gravitational energy fragment into a few pieces. Dependence on the other parameters is weak and is not observed clearly in our calculation. The physical explanation for this fragmentation condition is also presented.

How much angular momentum do initial cores have in reality? According to cosmological simulations by Yoshida et al. (2006), first-star forming cores have the rotation parameter $\beta \simeq 0.1$. In discussing the fragmentation condition, the rotation parameter near the center should be used rather than that averaged over the core. Matter in the outer part tends to have larger rotation energy than gravitational energy, the value of the rotation parameter β becomes larger if outer material is included in calculations. Even though the central value of the rotation parameter might be significantly smaller than 0.1 owing to this effect, it is probably higher than our threshold value for fragmentation ($10^{-5} - 10^{-6}$) with a wide margin. Therefore, most of the cores are expected to fragment and proto-binaries are formed even in primordial-gas clouds.

In Figure 14, we plot the separations between fragments R_{sep} at the end of the calculation against the fragmentation epoch n_f for all the models where fragmentation is observed. The large crosses show ranges of fragmentation epochs (horizontal) and fragmentation scales (vertical) for models with $\beta_0 > 0.02$ (dotted line) ($\beta_0 < 0.02$, solid line, respectively). The Jeans length (left axis) and gas temperature (right axis) are also shown. We can see that the separation between fragments is approximately equal to the Jeans length at the fragmentation. Another striking feature is that fragmentation densities are clustered in two epochs of $n \approx 10^{12} \text{ cm}^{-3}$ and 10^{21} cm^{-3} . Cores with rapid rotation ($\beta_0 > 0.02$; symbols ‘+’) fragment in the earlier epoch ($n_c \simeq 10^{10} - 10^{14} \text{ cm}^{-3}$) with larger separation $\simeq 10 - 1000 \text{ AU}$, while those with slower rotation ($\beta_0 < 0.02$; symbols ‘×’) in the later epoch ($n_c \simeq 10^{18} - 10^{21} \text{ cm}^{-3}$) with smaller separation $\simeq 0.01 - 1 \text{ AU}$. These two fragmentation epochs have their origin in thermal evolution of primordial gas. The lower-density fragmentation is a result of a temperature drop owing to the three-body H_2 formation at $n_c \simeq 10^{10} \text{ cm}^{-3}$, while the higher-density one results from another temperature drop at $n_c \simeq 10^{17} \text{ cm}^{-3}$, owing to the H_2 collision-induced cooling. Recall that a quasi-rotation supported disk can continue to collapse for $\gamma < 1$ while conserving angular momentum. Thus even if collapse of the disk is about

to halt, the disk can collapse further owing to the temperature drops. Such disks stop their collapse and fragment when the temperature starts increasing again. It is known that these two cooling mechanisms do not cause fragmentation of the core by simple thermal instability (Omukai & Yoshii 2003; Ripamonti & Abel 2004). In our case, where a disk is present, these cooling mechanisms result in the fragmentation of the disk.

There is a caveat in our results on fragmentation epochs. We adopted the equation of state derived from one-zone calculation. For example, the temperature variation in one-zone models tends to be exaggerated: the two temperature dips are deeper than in hydrodynamical calculations (e.g., Omukai & Nishi 1998). In addition, in hydrodynamical models, temperature in the envelope tends to be higher than that in the center for the same density (Whitehouse & Bate 2006; Stamatellos et al. 2007). Despite these possible differences, we expect that the fragmentation condition itself (eq. 8) remains valid. In deriving this condition (Sec. 6), we only assumed that once a quasi-rotation supported disk forms, it eventually fragments. This is correct if the EOS has a sufficiently large density range with $\gamma > 1$, which is indeed the case in the primordial gas. In fact, in the context of present-day star formation, the same fragmentation criterion has been reported (Matsumoto & Hanawa 2003; Machida et al. 2005b). On the other hand, the fragmentation epoch and scale can be subject to change if EOS is altered.

Although the majority of cores are predicted to fragment before the stellar core formation, whether they finally evolve into bona fide binaries/multiples remains obscure. The separation between fragments changes significantly during the mass accretion phase as a result of angular momentum influx to the fragments. An accreted gas in a later stage tends to have a larger specific angular momentum, while spiral arms in a density pattern, which transfer angular momentum outward, might be invoked in such a phase. To answer whether fragments evolve into binaries/multiples or merge into a single star, we need to extend calculations over the entire accretion phase.

When more than two fragments appear (e.g., models 1 and 2 in Fig. 3), some might be ejected from the parental core as a result of three-body interactions (Bate et al. 2002, 2003). Ejected objects stop gaining mass by accretion thereafter. By this mechanism, a spectrum in mass of metal-free stars might be formed. For example, if an ejection event takes place in the very early accretion phase, the ejected object can eventually evolve into a metal-free brown dwarf. Or if a stellar core with its envelope of $\sim 1 M_{\odot}$ is ejected, a low-mass metal-free star is the outcome. Considering the origin of the two hyper metal-poor ($[\text{Fe}/\text{H}] < -5$) stars (Christlieb et al. 2001; Frebel et al. 2005), Suda et al. (2004) showed that their abundance patterns can be explained by nucleosynthesis and mass transfer in first-generation low-mass binary stars. In our scenario, such a system can be formed naturally. In some models (e.g.,

see Fig. 3*a* and *b*), multiple pairs of binaries appear. If one such pair is ejected from the parental core, it would result in a low-mass metal-free binary system.

With neither ejection nor merging to a single star, our binary systems of fragments are expected to become very massive star binaries. Such systems are considered to be important sources of gravitational waves (Belczynski et al. 2004). Also they can be gamma-ray burst progenitors if formed in close binaries (Bromm & Loeb 2006; Yoon et al. 2006).

In this study, we did not include magnetic effects. According to recent studies, however, a low level of magnetic field could be present even in the early universe (Langer et al. 2003; Ichiki et al. 2006). If an initial primordial-gas core has $B > 10^{-13.5}$ G of the magnetic field, a protostellar jet is launched (Machida et al. 2006c), and this jet significantly affects the mass accretion process. Even with a lower level, a magnetic field can suppress fragmentation of the core, by transferring angular momentum via magnetic braking (e.g., Machida et al. 2007; Price & Bate 2007). So far those effects on primordial star formation have been largely overlooked. Further studies along this line are clearly needed in future.

We have greatly benefited from discussion with H. Susa, T. Tsuribe, and K. Saigo. We also thank T. Hanawa for contribution to the nested grid code. Numerical computations were carried out on VPP5000 at Center for Computational Astrophysics, CfCA, of National Astronomical Observatory of Japan. This work is supported by the Grant-in-Aid for the 21st Century COE "Center for Diversity and Universality in Physics" from the Ministry of Education, Culture, Sports, Science and Technology (MEXT) of Japan, and partially supported by the Grants-in-Aid from MEXT (15740118, 16077202, 18740104, 18740113).

REFERENCES

- Abel, T., Bryan, G. L., & Norman, M. L. 2002, *Science*, 295, 93
- Basu S., & Moushovias T. Ch., 1994, *ApJ*, 432, 720
- Bate, M. R., Bonnell, I. A., & Bromm, V. 2002, *MNRAS*, 336, 705
- , 2003, *MNRAS*, 339, 577
- Belczynski, K., Bulik, T., & Rudak, B. 2004, *ApJ*, 608, L45
- Belczynski, K., Bulik, T., Heger, A. & Fryer, C. 2006, *ApJ*, submitted (astro-ph/0610014)
- Bonnor, W. B. 1956, *MNRAS*, 116, 351

- Bromm, V., Coppi, P. S., & Larson, R. B. 1999, *ApJ*, 527, L5
- , 2002, *ApJ*, 564, 23
- Bromm, V., & Loeb, A. 2006, *ApJ*, 642, 382
- Bromm, V., & Larson, R. B. 2004, *ARA&A*, 42, 79
- Christlieb, N., Green, P. J., Wisotzki, L., & Reimers, D. 2001, *A&A*, 366, 898
- Clark, P. C., Glover, S. C. O., & Klessen, R. S. (2007), submitted to *ApJ* [arXiv:0706.0613 (astro-ph)]
- Duquennoy, A., & Mayor, M. 1991, *A&A*, 248, 485
- Ebert, R. 1955, *Z. Astrophys.*, 37, 222
- Fischer, D. A., & Marcy, G. W. 1992, *ApJ*, 396, 178
- Frebel, A., et al. 2005, *Nature*, 434, 871
- Hanawa, T., & Matsumoto, T. 1999, *ApJ*, 521, 703
- Hanawa, T., & Matsumoto, T. 2000, *PASJ*, 52, 241
- Ichiki, K., Takahashi, K., Ohno, H., Hanayama, H., & Sugiyama, N., 2006, *Science*, 311, 787
- Langer, M., Puget, J.-L., & Aghanim, N. 2003, *Phys. Rev. D*, 67, 043505
- Larson R. B., 1969, *MNRAS*, 145, 271
- Lai, D. 2000, *ApJ*, 540, 946
- Machida, M. N., Tomisaka, K., & Matsumoto, T. 2004, *MNRAS*, 348, L1
- Machida, M. N., Matsumoto, T., Tomisaka, K., & Hanawa, T. 2005a, *MNRAS*, 362, 369
- Machida, M. N., Matsumoto, T., Hanawa, T., & Tomisaka, K. 2005b, *MNRAS*, 362, 382
- Machida, M. N., Matsumoto, T., Hanawa, T., & Tomisaka, K. 2006a, *ApJ*, 645, 1227
- Machida, M. N., Omukai, K., Matsumoto, T., & Inutsuka, S., 2006c, *ApJ*, 647, L1
- Machida, M. N., Inutsuka, S., & Matsumoto, T., 2007 *ApJ*, submitted (astro-ph/0702183)
- Matsumoto, T., Hanawa, T., & Nakamura, F. 1997, *ApJ*, 478, 569

- Matsumoto, T., & Hanawa, T. 1999, *ApJ*, 521, 659
- Matsumoto T., & Hanawa T., 2003, *ApJ*, 595, 913
- Matsumoto, T., & Tomisaka, K. 2004, *ApJ*, 616, 266
- Nakamura, F., & Hanawa, T. 1997, *ApJ*, 480, 701
- Omukai, K. & Nishi, R. 1998, *ApJ*, 508, 141
- Omukai, K., & Yoshii, Y., 2003, *ApJ*, 599, 746
- Penston M. V. 1969, *MNRAS*, 144, 425
- Price, D. J., & Bate M. R., 2007, *astro-ph/0702410*
- Ripamonti, E., & Abel, T. 2004, *MNRAS*, 348, 1019
- Stamatellos, D., Whitworth, A. P., Bisbas, T., & Goodwin, S., 2007, *A&A*, submitted (*astro-ph/0705.0127*)
- Saigo, K., Matsumoto, T., & Hanawa, T. 2000, *ApJ*, 531, 971
- Saigo, K., Matsumoto, T., & Umemura, M. 2004, *ApJ*, 615, L65
- Suda, T., Aikawa, M., Machida, M. N., Fujimoto, M. Y., & Iben, I. J. 2004, *ApJ*, 611, 476
- Takahashi, K., Ichiki, K., Ohno, H., & Hanayama, H. 2005, *Phys. Rev. Lett.*, 95, 121301
- Tohline, J. E. 1980, *ApJ*, 239, 417
- Tomisaka K. 2002, *ApJ*, 575, 306
- Truelove J. K., Klein R. I., McKee C. F., Holliman J. H., Howell L. H., & Greenough J. A., 1997, *ApJ*, 489, L179
- Tsuribe T., Omukai K., 2006, *ApJ*, 642, L61
- Whitehouse S. C., & Bate M. R., 2006, *MNRAS*, 367, 32
- Yoshida N., Omukai K., Hernquist L., & Abel T., 2006, *ApJ*, 652, 6
- Yoon, S.-C., Langer, N., & Norman, C., 2006, *A&A*, 460, 199

Table 1: Model parameters and calculation results

Model	β_0	A_ϕ	$\alpha_0 (f)$	$n_f (\text{cm}^{-3})^a$	NF ^b	Sep. ^c	Mode ^d
1	0.1	10^{-3}	0.7 (1.20)	1.62×10^{11}	8	870	R
2	0.1	0.01	0.7 (1.20)	1.76×10^{11}	6	625	R
3	0.1	0.1	0.7 (1.20)	1.95×10^{11}	2	335	R
4	0.1	0.3	0.7 (1.20)	3.47×10^{11}	8	163	B
5	0.01	10^{-3}	0.83 (1.01)	4.34×10^{18}	4	0.722	R
6	0.01	0.01	0.83 (1.01)	7.08×10^{18}	2	0.385	R
7	0.01	0.1	0.83 (1.01)	7.25×10^{18}	2	0.377	B
8	0.01	0.3	0.83 (1.01)	1.89×10^{19}	2	0.463	B
9	10^{-3}	10^{-3}	0.83 (1.01)	2.31×10^{18}	6	0.632	R
10	10^{-3}	0.01	0.83 (1.01)	2.66×10^{18}	2	0.292	R
11	10^{-3}	0.1	0.83 (1.01)	3.03×10^{18}	2	0.314	R
12	10^{-3}	0.3	0.83 (1.01)	7.43×10^{19}	5	0.476	B
13	10^{-4}	10^{-3}	0.83 (1.01)	7.54×10^{18}	4	0.419	R
14	10^{-4}	0.01	0.83 (1.01)	7.78×10^{18}	4	0.714	R
15	10^{-4}	0.1	0.83 (1.01)	7.99×10^{18}	2	0.097	B
16	10^{-4}	0.3	0.83 (1.01)	3.25×10^{21}	3	0.245	R
17	10^{-5}	10^{-3}	0.83 (1.01)	4.03×10^{20}	4	0.117	R
18	10^{-5}	0.01	0.83 (1.01)	5.92×10^{20}	6	0.087	R
19	10^{-5}	0.1	0.83 (1.01)	4.77×10^{20}	4	0.115	R
20	10^{-5}	0.3	0.83 (1.01)	3.53×10^{21}	2	0.031	R
21	10^{-6}	10^{-3}	0.83 (1.01)	—	1	—	—
22	10^{-6}	0.01	0.83 (1.01)	—	1	—	—
23	10^{-6}	0.1	0.83 (1.01)	—	1	—	—
24	10^{-6}	0.3	0.83 (1.01)	—	1	—	—
25	10^{-3}	0.01	0.2 (4.19)	4.62×10^{20}	4	0.163	B
26	10^{-3}	0.01	0.4 (2.10)	6.24×10^{20}	4	0.298	B
27	10^{-3}	0.01	0.6 (1.40)	1.76×10^{21}	4	0.492	R
28	10^{-3}	0.01	0.8 (1.05)	2.41×10^{21}	2	0.330	R
29	0.02	0.01	0.6 (1.40)	1.26×10^{18}	2	0.720	R
30	0.04	0.01	0.6 (1.40)	2.46×10^{14}	4	23.4	R
31	0.06	0.01	0.6 (1.40)	3.10×10^{12}	4	119	R
32	0.08	0.01	0.6 (1.40)	5.03×10^{11}	4	328	R
33	0.2	0.01	0.6 (1.40)	5.23×10^9	—	1.22×10^3	R
34	0.02	0.1	0.6 (1.40)	7.16×10^{19}	2	0.209	B
35	0.04	0.1	0.6 (1.40)	2.29×10^{14}	4	28.8	R
36	0.06	0.1	0.6 (1.40)	3.21×10^{12}	4	113	R
37	0.08	0.1	0.6 (1.40)	5.51×10^{11}	4	344	R
38	0.2	0.1	0.6 (1.40)	5.38×10^9	—	1.21×10^3	R

^a number density at fragmentation epoch, ^b number of fragments, ^c the separation between furthest fragments, ^d fragmentation mode (R: ring, B: bar).

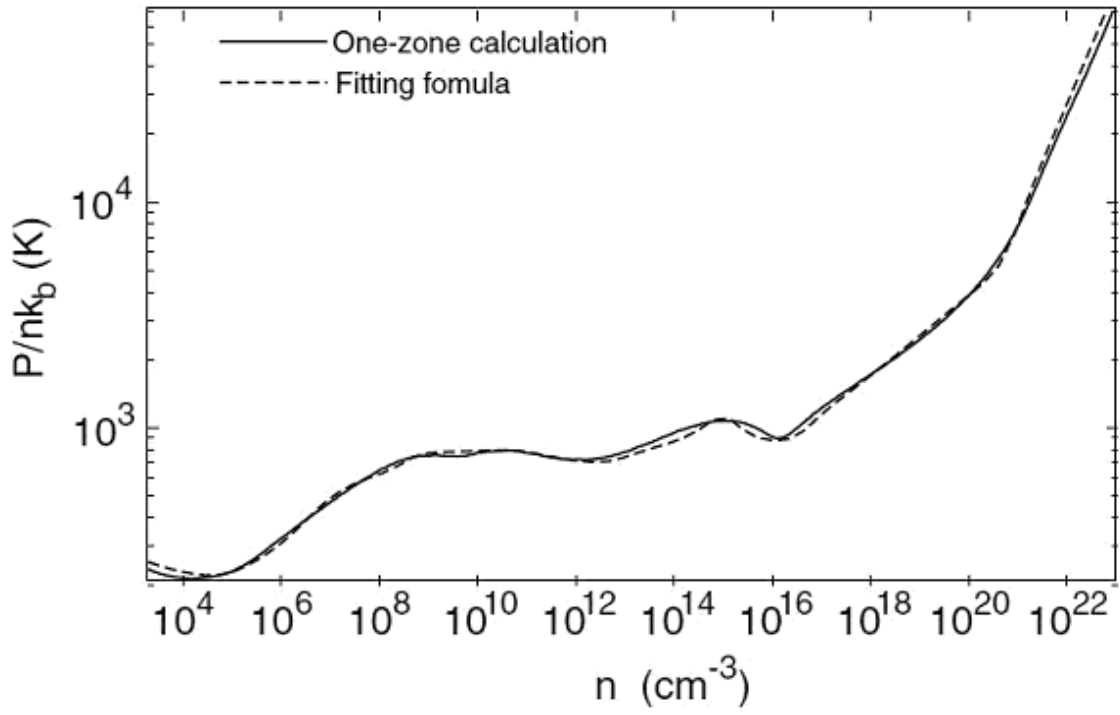


Fig. 1.— Gas pressure normalized by number density derived from a one-zone calculation (solid) and our fit used in the numerical simulation (dashed line).

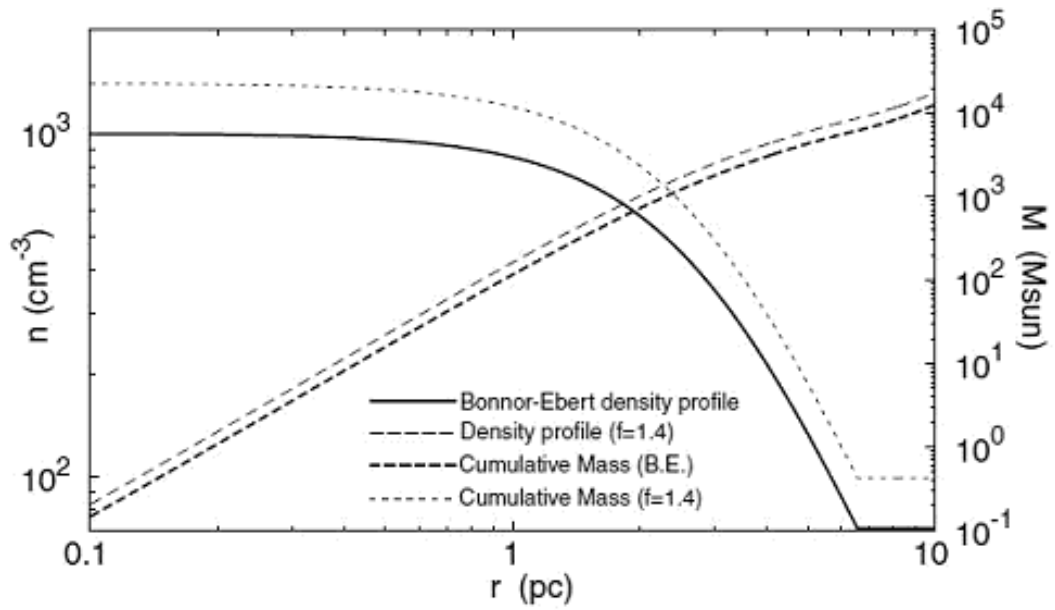


Fig. 2.— The density (*thick solid line*) and enclosed mass (*thick dashed line*) distribution for the critical Bonnor-Ebert sphere as a function of the radius. Those increased by a factor $f=1.4$ are also plotted by the thin lines.

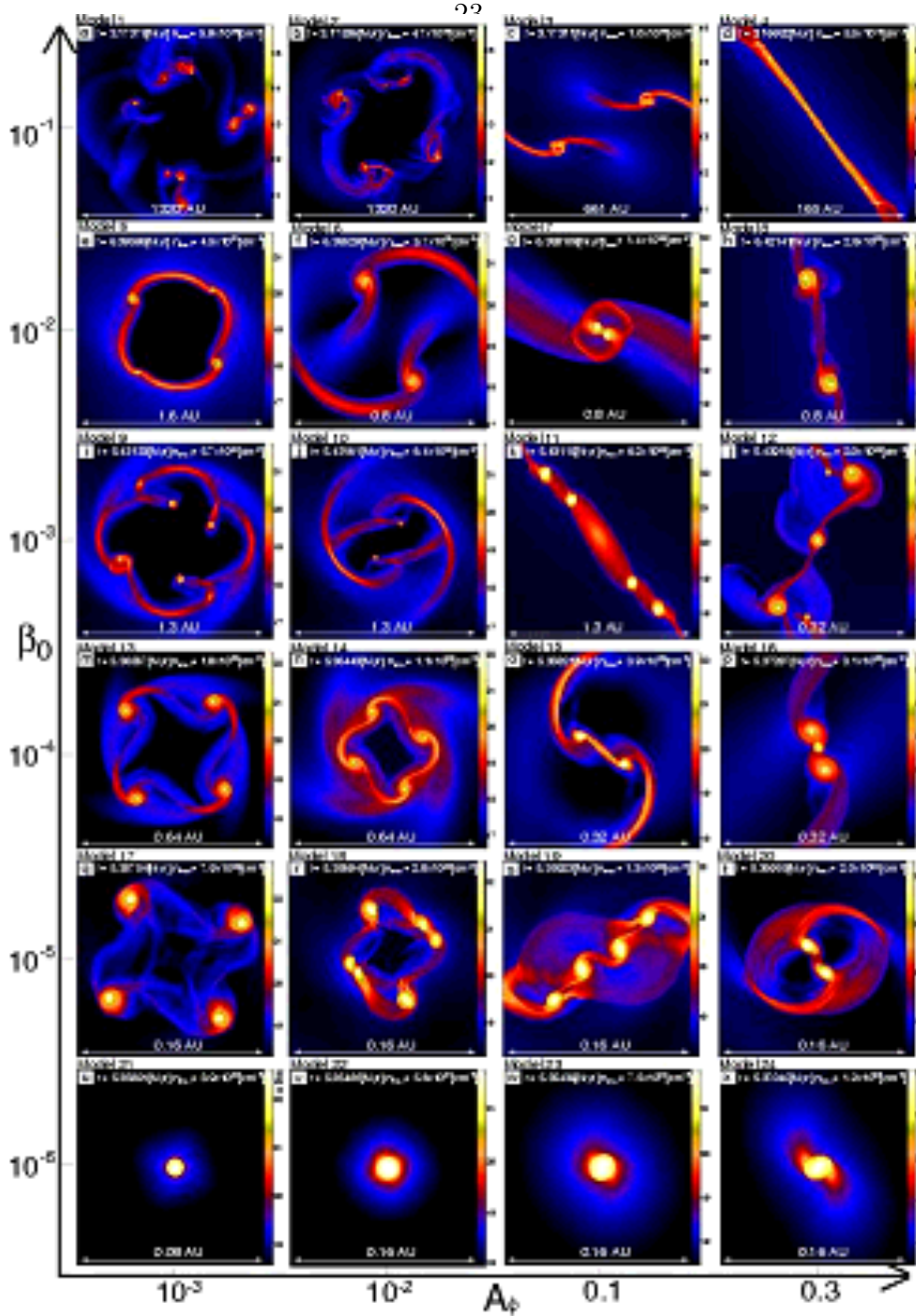


Fig. 3.— The collapse outcome of primordial-gas cores with different initial rotation parameter β_0 and amplitude of non-axisymmetric (bar-mode) perturbation A_ϕ . The final states in our calculation for models 1-24 in Table 1, where the cores are close to hydrostatic initially, i.e., $\alpha_0 \sim 1$ are presented. Shown by false colors is the density distribution around the center on the plane perpendicular to the rotation axis. The model numbers are denoted on the upper-left corners of the panels. The name of the panel (a-x), the time elapsed since the beginning of the calculation t , the maximum number density attained n_{\max} are given at the top, and the box scale is shown at the bottom of the panel.

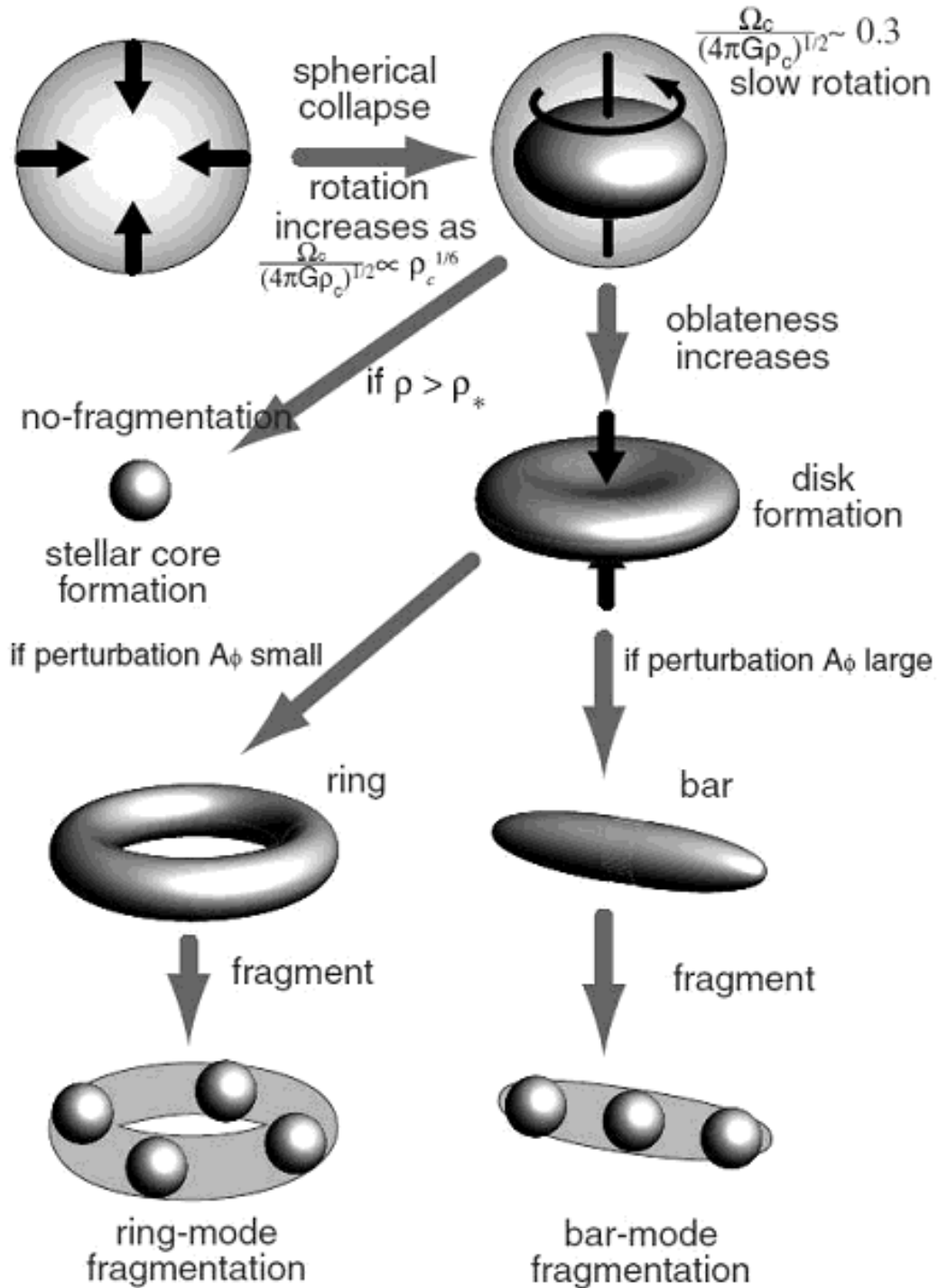


Fig. 4.— A schematic for the evolution of rotating cores. If the core reaches the stellar density ρ_* before the disk formation, it does not fragment. Otherwise, it fragments in the bar mode or ring mode depending on the amplitude of the bar-mode perturbation at the time of disk formation.

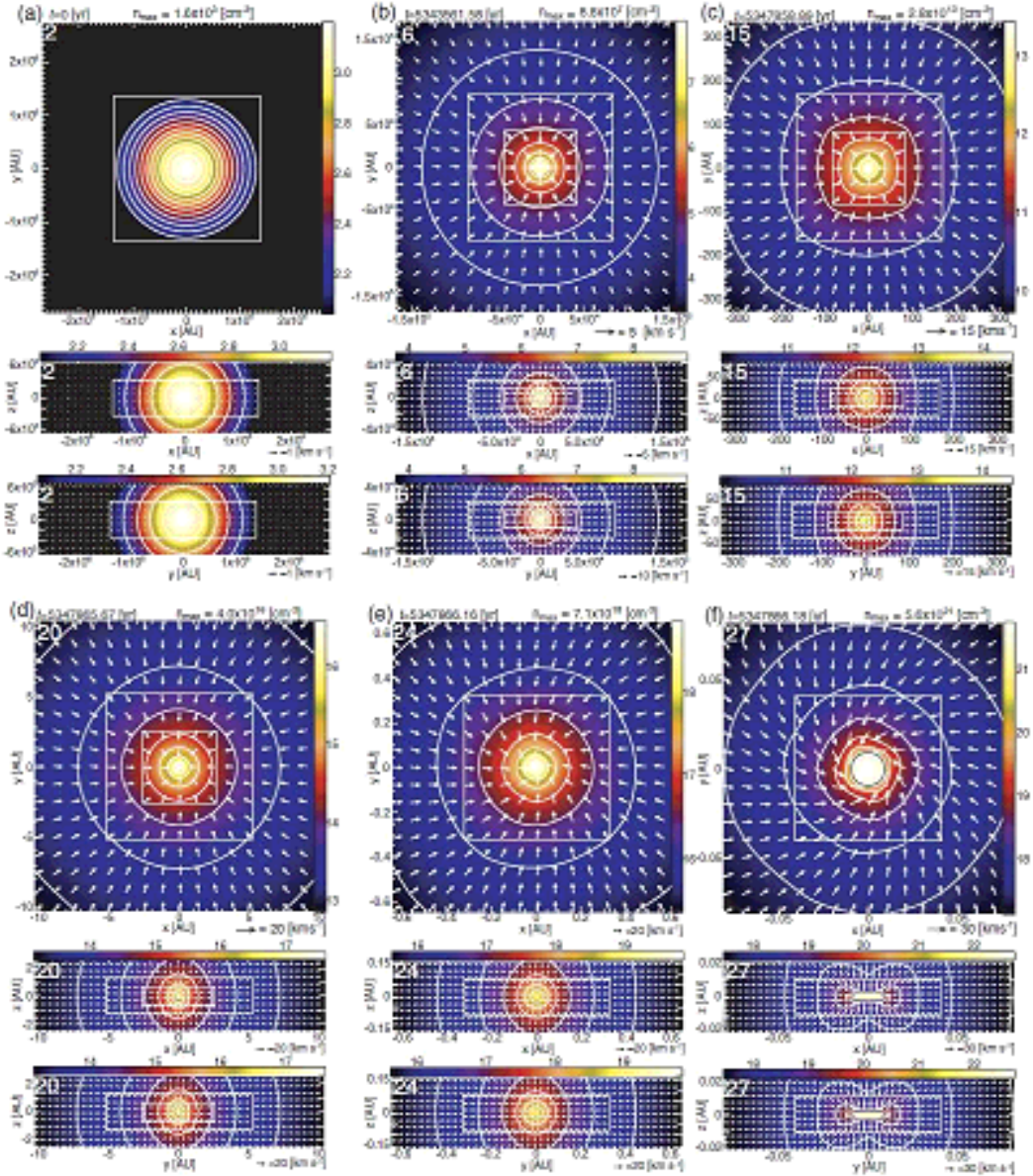


Fig. 5.— The density (*color scale and contour*) and velocity (*arrows*) distributions at six different epochs in model 22 $[(\alpha_0, \beta_0, A_\phi) = (0.83, 10^{-6}, 10^{-2})]$. The upper, middle, and lower panels show those on $x - y$, $x - z$, and $y - z$ planes, respectively. The elapsed time, maximum density (above) and arrow scale (below) are denoted above or below each panel. The level of the grid is indicated in the upper left corner of each panel. Solid squares in each panel are outer boundaries of subgrids. The structure around the center is zoomed up from Panel *a* toward *f*. The grid size of Panel *a* (the coarsest grid shown is $l = 2$) is 6.7×10^6 AU, while that of Panel *f* ($l = 27$) is 0.2 AU, 2^{25} times finer than in Panel *a*. The black contour in Panel *f* denotes the constant density surface of $n = 10^{20} \text{ cm}^{-3}$, approximately corresponding to the surface of the stellar core.

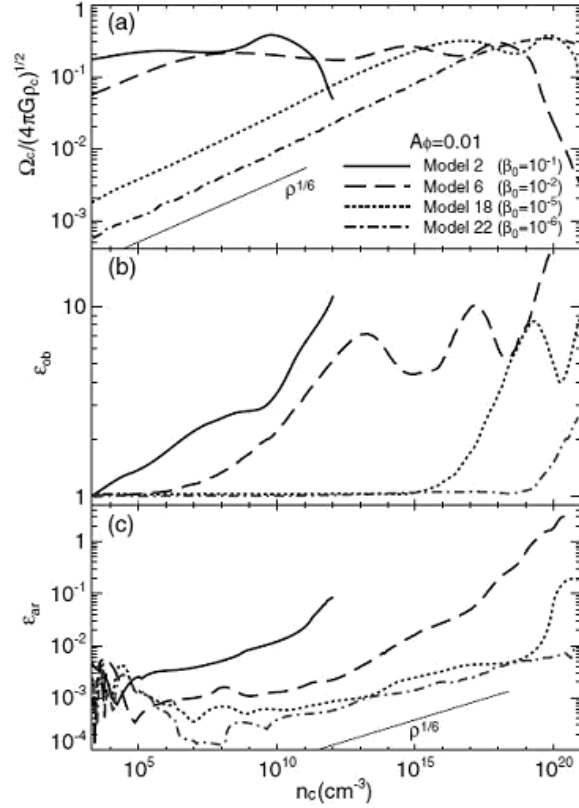


Fig. 6.— Evolution of (a) the central normalized angular velocity ω_c , (b) oblateness ε_{ob} and (c) axis ratio ε_{ar} of the cores as a function of the central number density n_c . Four cases (models 2, 6, 18 and 22 in the second column of Figure 3) with the same initial non-axisymmetric perturbation $A_\phi = 0.01$ but with different rotation parameters ($\beta_0 = 10^{-6} - 10^{-1}$) are shown. The dash in Panel (a) shows the growth rate for the spherical collapse, while that in Panel (c) indicates the growth rate in the isothermal case by the linear analysis.

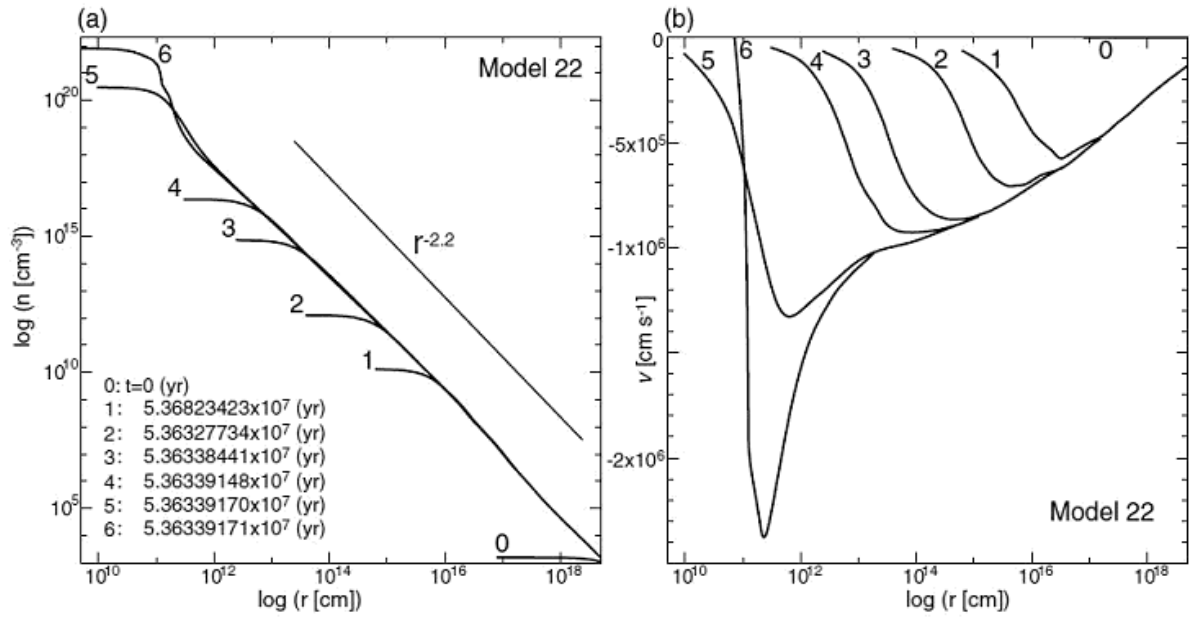


Fig. 7.— The radially averaged (a) number density and (b) velocity profiles at different epochs in model 22. The time for each plot is indicated in panel *a*. The dash in panel *a* shows the relation $n \propto r^{-2.2}$.

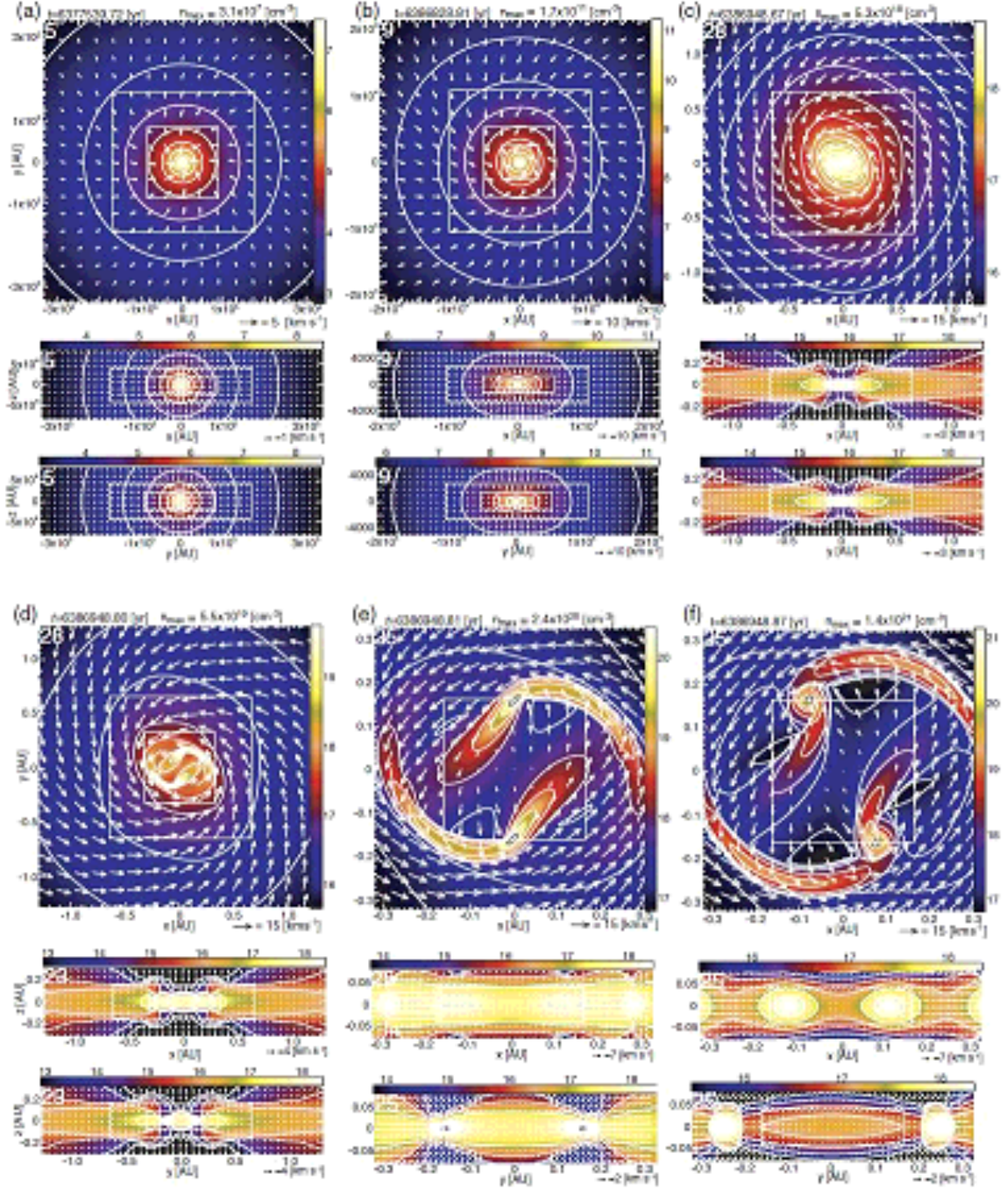


Fig. 8.— The same as Fig. 5 but for model 6 with $(\alpha_0, \beta_0, A_\phi) = (0.83, 10^{-2}, 0.01)$.

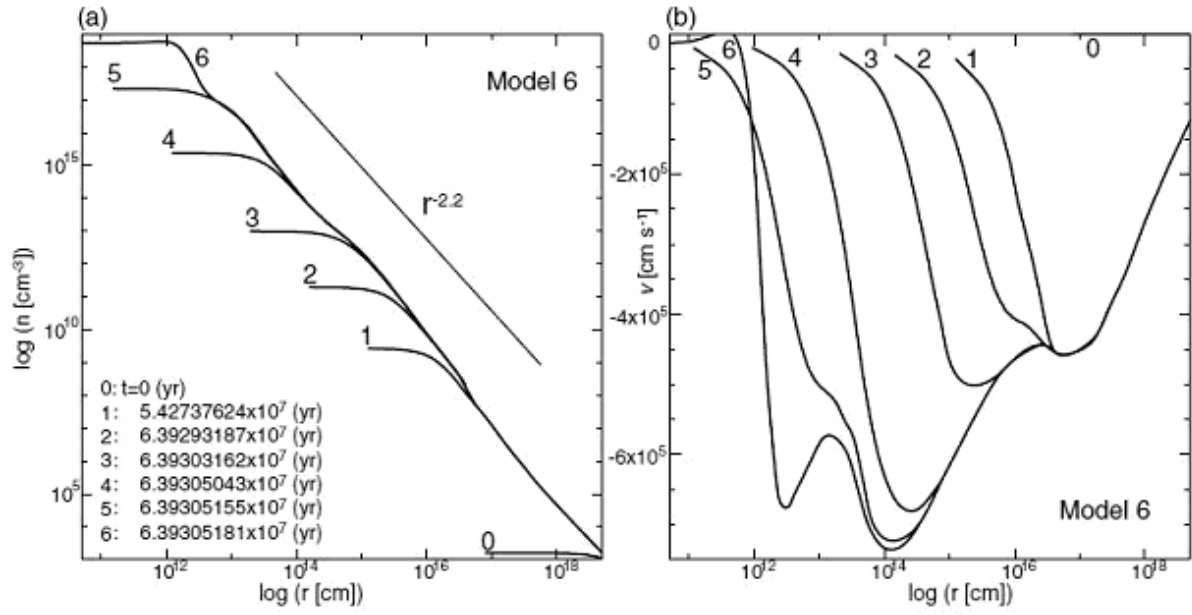


Fig. 9.— The same as Figure 7 but for model 6.

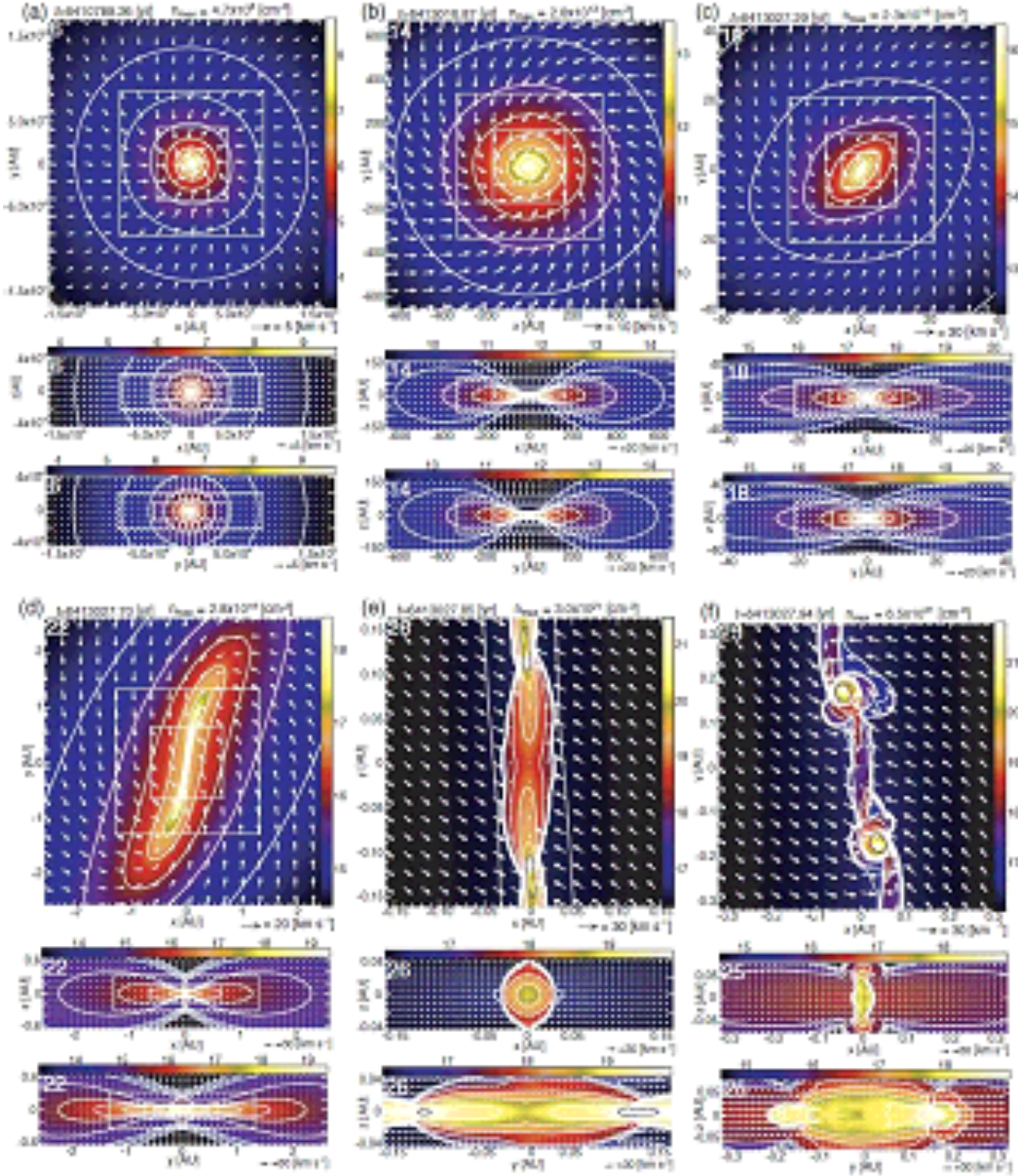


Fig. 10.— The same as Fig. 5 but for model 8 with $(\alpha_0, \beta_0, A_\phi) = (0.83, 10^{-2}, 0.3)$.

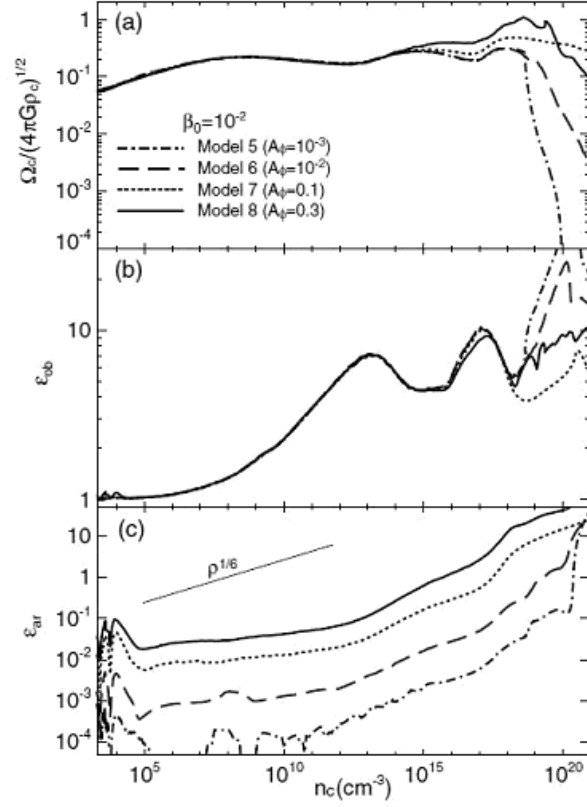


Fig. 11.— The same as Figure 6 but for cases with same initial rotation parameter $\beta_0 = 10^{-2}$ with different amplitude of initial non-axisymmetric perturbation $A_\phi = 0.01$ (models 5, 6, 7 and 8, in the second row of Figure 3).

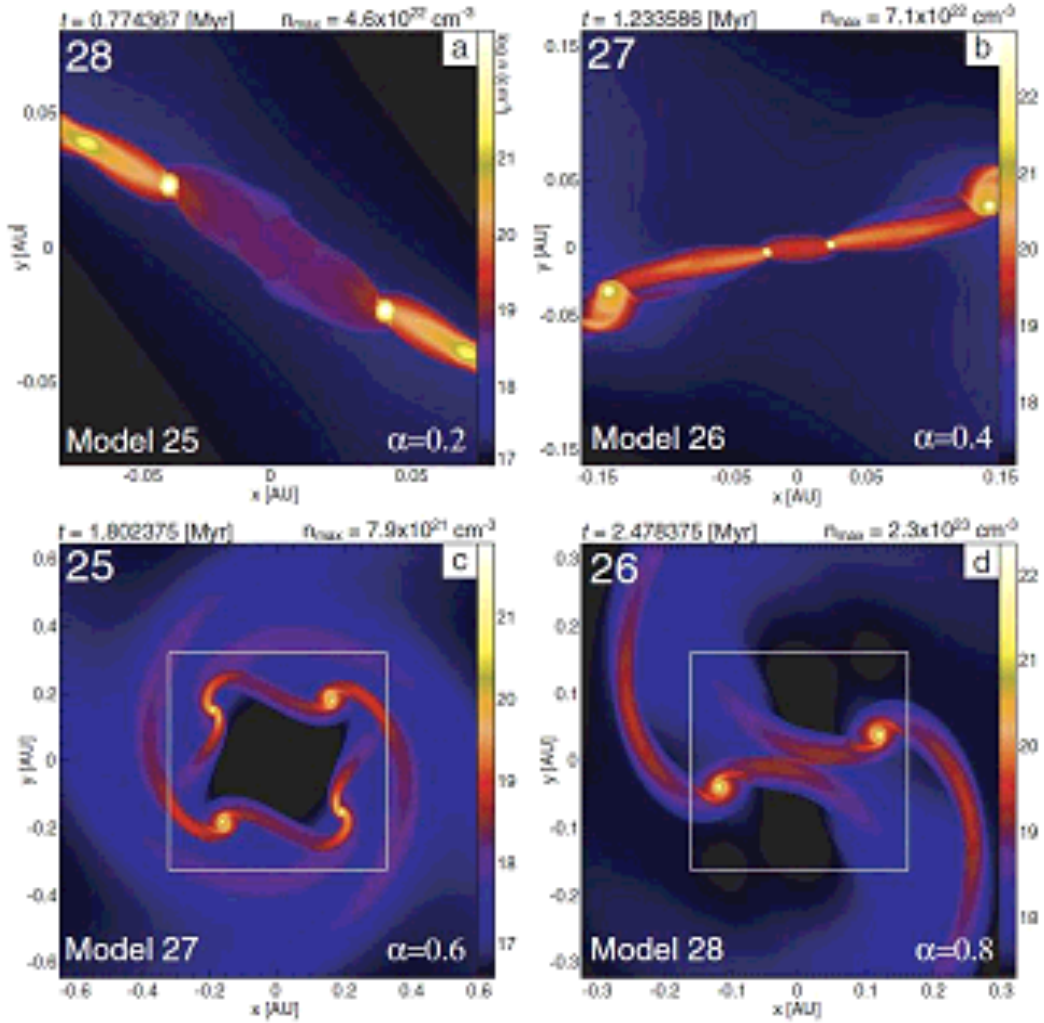


Fig. 12.— The collapse outcome of highly gravitationally unstable cores (models 25-28). The values of α_0 are indicated in the bottom-left corner of the panels. The legend is the same as in Figure 5.

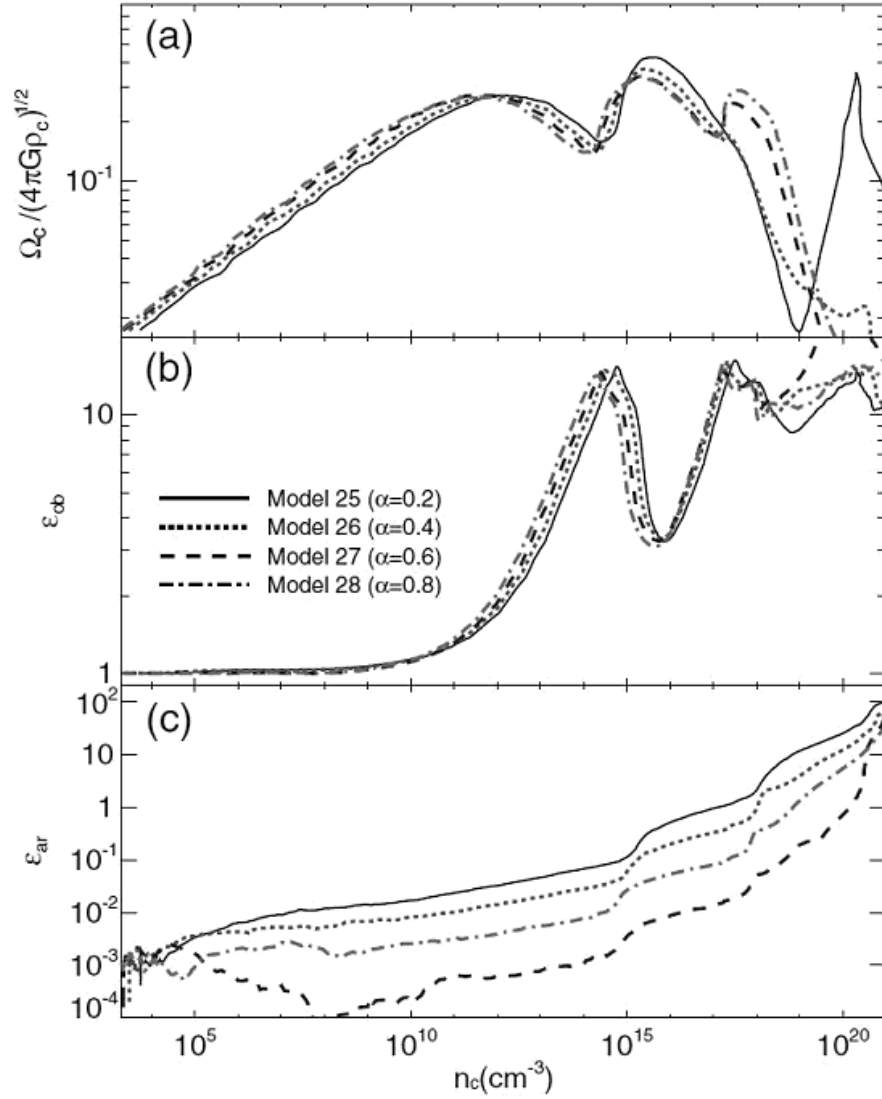


Fig. 13.— The same as Figure 6 but for highly gravitationally unstable cores (models 25-28). The values of α_0 are indicated in panel (b).

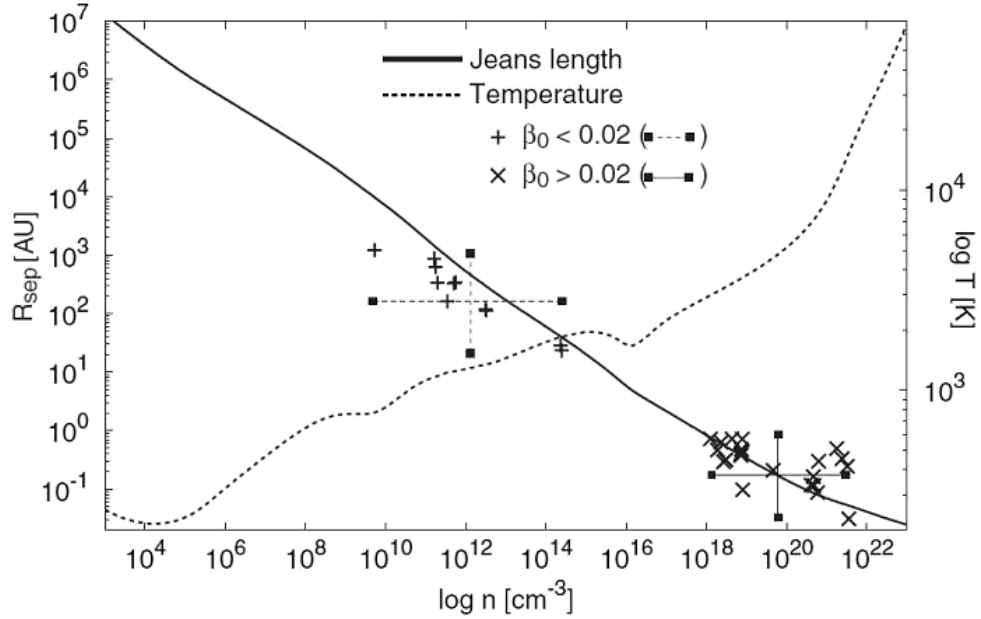


Fig. 14.— The separations between fragments against the density at fragmentation. We adopt the separation between furthestmost fragments if more than two fragments appeared. The evolution of temperature (right) and Jeans length (left) is also illustrated by the dotted and solid lines, respectively. The results of all the models where fragmentation is observed are plotted. Those with the rotation parameter $\beta_0 > 0.02$ (< 0.02) are shown by symbols ‘+’, (‘x’, respectively). The large dotted (solid) cross represents the range of the fragment separation and fragmentation epoch for cases with $\beta_0 > 0.02$ (< 0.02 , respectively).